# Measurements and modeling of a monolithically integrated self-spiking two-section laser in InP

# Measurements and Modeling of a Monolithically Integrated Self-Spiking Two-Section Laser in InP

Lukas Puts, Daan Lenstra, *Life Senior Member, IEEE*, Kevin Williams, *Member, IEEE*, and Weiming Yao, *Member, IEEE*

***Abstract*— The self-spiking behavior of an integrated saturable absorber and gain section laser fabricated in an InP technology platform is analyzed. The gain, absorber and intensity dynamics are first inspected using the normalized Yamada model. This model shows excitable behavior as well as the relative refractory period, both of which are also present in biological neurons. Measurements of a two-section laser show irregular spike generation on the millisecond timescale, with a saturable absorber voltage controlled spike density. From our simulations, and from the quasi-random character and millisecond timescale at which these pulses occur, we conclude the laser is triggered by noise, an important characteristic in the operation of biological neurons. Simulations of the laser around the excitability threshold using a newly proposed model with an optical noise term show qualitatively similar self-spiking behavior as measured.**

***Index Terms*— Bistable laser, Yamada model, optical noise, optical neuron, spiking neuron.**

## I. Introduction

AFTER two periods of setbacks in the '70s and '80s, research into artificial intelligence (AI) is experiencing a steady growth since the beginning of the 21st century. The reason for this revival was the improvement in computational power in microprocessors. In recent years, research into AI is experiencing an exponential growth, mainly driven by novel algorithms, neural network modeling, big data and the predictions of the end of Moore's Law [1].

Currently, neural network models are implemented in software frameworks such as Tensorflow to build large deep neural networks (DNNs). Such networks consist of artificial neurons arranged in multiple layers, each applying a filtering operation on input data. Since neurons are densely interconnected, calculations in these networks are performed in a parallel manner. These models are often trained and put into practice using conventional electronic hardware such as CPUs and GPUs. These processors are build following the Von-Neumann architecture, where data processing and memory units are physically separated. The CPU fetches instructions from its memory unit on every clock cycle, processes the input data, and then generates the output. Thus, data is processed sequentially. This serial way of processing limits the speed at which parallel computations can be done.

Another limiting factor in electronics is power dissipation, mainly driven by electrical interconnects. The skin effect, dielectric losses, and wiring density all add to power dissipation [2], [3]. This energy consumption of electronic hardware for AI calculations is an important factor to consider. Electronic neuromorphic processors such as IBM's neurosynaptic core and Neurogrid are optimized from an architectural perspective, but still face speed and interconnection challenges due to the fundamental bandwidth fan-in tradeoff [3]. The limited bandwidth of electronic solutions also restricts the operational speed. For low-speed application such as image recognition in the kHz regime, the operational speed of electronics is sufficient, however, tasks such as manipulating the radio spectrum for hypersonic aircraft must be performed in the GHz regime [1], and fiber non-linearity compensation, model predictive control, and high-energy particle classifications need low-latency solutions [4].

The most energy efficient neural network is the human brain, where data is encoded using short electrical signals or spikes. These spikes are digital in amplitude but analogue in the time domain, and are generated by individual neurons and transmitted through axons [3]. In [5], an extensive comparison between the human brain and digital computing in terms of energy efficiency is given. The combined analogue and digital data representation scheme allows for a less strict error tolerance compared to digital computers. In digital computers, the error probability is around $10^{-24}$, whereas for the human brain, this value is estimated to be around 0.65. This means that the human brain with its spiking neural network operates in an incredibly noisy environment. However, the human brain is optimized such that it operates at an energy efficiency almost 60 times greater than digital computers, at only 20 Watts.

The principles of a biological spiking neural network (SNN) can be transferred to integrated photonics due to the spiking capabilities of integrated lasers [6], [7], [8]. Integrated photonics benefits from high switching speed, high communication bandwidth, low crosstalk [9], [10], and temporal characteristics governed by ultra-fast carrier dynamics [11]. This means that an optical neuron might operate orders of magnitude faster than its biological counterpart and can be the non-linear building block in an all-optical spiking neural network

Manuscript received 1 August 2022; revised 24 October 2022; accepted 31 October 2022. Date of publication 24 November 2022; date of current version 24 May 2023. This work was supported by the Netherlands Organization for Scientific Research (NWO) through the project 'Light up the brain: accelerating AI research with integrated photonics (17269)' and the Zwaartekracht Grant 'Research Center for Integrated Nanophotonics'. *(Corresponding author: Lukas Puts.)*

The authors are with the Photonic Integration Group, Department of Electrical Engineering, Eindhoven University of Technology, 5600 MB Eindhoven, The Netherlands (e-mail: l.puts@tue.nl).

Color versions of one or more figures in this article are available at https://doi.org/10.1109/JQE.2022.3224786.

Digital Object Identifier 10.1109/JQE.2022.3224786


Fig. 1. Schematic overview of a laser with saturable absorber and gain section laser. The absorber and gain elements are surrounded by mirrors R to create an optical cavity.

on a photonic integrated circuit (PIC). There are several challenges in realizing an all-optical SNN. Next to research into the non-linear neuron [12], [13] also low-energy synaptic weighting and scalable neuromorphic architectures that allow for efficient training are being investigated [14]. Synaptic weighting can be performed using a single photonic ring resonator [15] and can be scaled up by increasing the number of resonators to form a weight bank [16] and leveraging the benefits of wavelength division multiplexing (WDM) [10]. Another approach is by using phase changing materials (PCM) to manipulate the transmission of waveguides [17], [18].

In this work, we are addressing the excitable nonlinearity [19], [20] within an SNN and in specific how lasers can be used as a self-spiking source and analyze its characteristics. Given the fact that the human brain operates in an incredibly noisy environment, it is essential to identify the effects of optical noise on its photonic counterpart. The influence of noise on a self-pulsating two-section laser has been studied before in terms of timing statistics, jitter and amplitude variations [19], [21]. This shows that noise is an important aspect in the dynamics of a two-section laser. We report on an integrated saturable absorber and gain laser that shows quasi-random self-spiking in the presence of noise. We adapted the well-known Yamada model [3], [15], [22] to investigate the effects of optical noise on the laser's self-spiking behavior in simulations. To the best of our knowledge, this is the first time the self-spiking behavior of such a laser structure is investigated in the presence of optical noise in simulations and measurements.

## II. Theoretical Framework

The laser structure under investigation is a two-section laser comprising a saturable absorber and gain section (Figure 1). By including a loss mechanism in an optical cavity, the laser becomes bistable [23], [24], [25], [26] and as a result, the laser can exhibit various dynamical properties such as Q-switching, mode-locking, or a combination of both [27]. For example, a minor change of a few percent of the saturable absorber and gain length ratios and carrier lifetimes may already affect the stability, modulation depth and pulse width of a mode-locked laser [28]. In addition, also the time-bandwidth product and side mode suppression ratio depend on the saturable absorber and gain length ratio, as demonstrated in the InP technology platform [29]. Another dynamical property of these types of lasers is excitability. This refers to the state where the system, initially at rest, can be brought with an external trigger into a different state (such as a pulsating state) before it returns to its rest state. Similar dynamics are observed in biological neurons, where a stimulus must be of sufficient strength to trigger a neuron to fire [3]. This means that from an external source, either deterministic or random noise, the laser can

TABLE I
Normalized Yamada Model Parameter Description

| | | | |
|---|---|---|---|
| $G$ | Gain | $B$ | Level of absorption |
| $\gamma_G$ | Gain relaxation rate | $a$ | Differential absorption relative to differential gain |
| $A$ | Gain bias current | | |
| $I$ | Optical intensity | $\gamma_I$ | Inverse photon lifetime |
| $Q$ | Loss | $\varepsilon f(G)$ | Spontaneous emission |
| $\gamma_Q$ | Loss relaxation rate | $\theta$ | Optical injection |

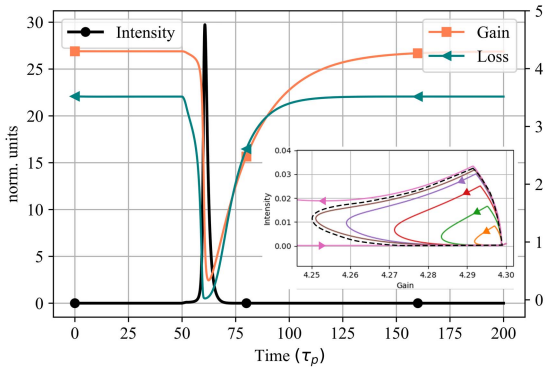


Fig. 2. Example of a pulse generation. At $t = 50\ \tau_p$, a small amplitude optical pulse is added to the model to trigger the laser. The parameters are $A = 4.3$, $\gamma_G = 0.05$, $\gamma_Q = 0.1$, $\gamma_I = 1$, $B = 3.52$, $a = 5$. The inset shows the corresponding $(G, I)$-phase diagram. Optical stimuli below the excitability threshold (indicated by the dashed line) result in short trajectories without an excitable response, whereas an optical stimuli above the threshold results in a very large excursion and pulse creation.

generate an optical spike or pulse. The intracavity loss element can be active such as an acoustic- or electro-optic modulator, or passive, such as a saturable absorber. In the last case, the laser dynamics are governed by the different carrier lifetimes in the gain and absorber region [25], which are on the order of hundreds and tens of picoseconds, respectively.

An optical pulse is formed if the absorber is bleached, i.e. if the losses are reduced significantly. This can be done by changing the absorption by means of carrier injection, or by increasing the intensity in the cavity by an optical trigger. The dynamical properties of such a laser can be described by the Yamada model, which has been extensively studied [19], [20], [25]. In this model, the gain, loss and intensity dynamics can be described by three coupled differential equations for the gain $G$, loss $Q$ and optical intensity $I$:

$$\frac{dG}{dt} = \gamma_G[A - G(t) - G(t)I(t)] \quad (1)$$

$$\frac{dQ}{dt} = \gamma_Q[B - Q(t) - aQ(t)I(t)] \quad (2)$$

$$\frac{dI}{dt} = \gamma_I[G(t) - Q(t) - 1]I(t) + \epsilon f(G) + \theta(t) \quad (3)$$

The parameter description is given in Table I. The time scale at which the solutions for $G$, $Q$, and $I$ are calculated using this model is in the unit of the photon lifetime $\tau_p$.

Figure 2 shows the response of $G$, $Q$ and $I$ (marked by squares, triangles and circles, respectively) under a deterministic optical pulse injection at $t = 50\ \tau_p$. Under steady-state conditions (i.e. $t < 50\ \tau_p$), only low-intensity spontaneous emission contributes to Eq. (3). Since $I$ is low, Eq. (1) and (2)

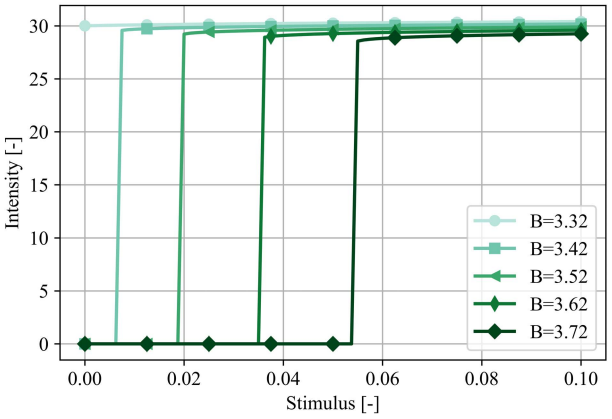


Fig. 3. Simulated threshold for five different absorption values and a fixed gain bias current A of 4.3.

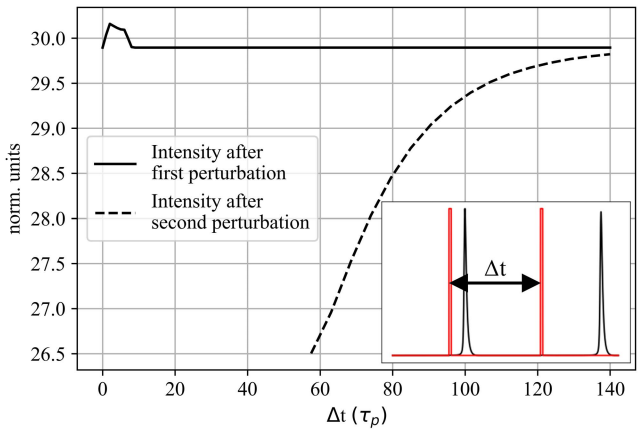


Fig. 4. Pulse amplitude after triggering but a short stimulus.

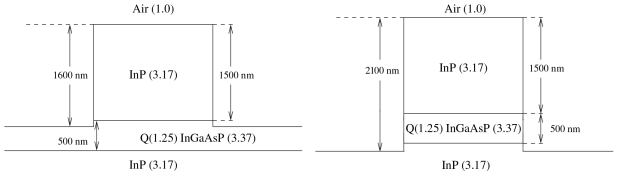


Fig. 5. Cross-section of the shallow (left) and deep (right) waveguide structures in the generic integration platform.

reduce to $\dot{G} = \gamma_G [A - G(t)]$ and $\dot{Q} = \gamma_Q [B - Q(t)]$, respectively, so the equations are dynamically decoupled and the system is at rest. At t = 50 $\tau_p$, an external optical pulse $\theta(t)$ is added to $I$, and the intensity starts to increase. Consequently, the losses rapidly decrease, and a very sharp increase in the optical intensity is formed. This depletes the gain and results in a reduction of intensity, forming a pulse. After the pulse formation, the gain and loss recover following their respective recovery rates to their steady-state conditions.

The model is used first to investigate the strength that is needed for the optical pulses to achieve an excitable response. Figure 3 shows the simulated pulse intensity amplitude for five values of the absorption $B$, a fixed value of 4.3 for gain bias $A$ and optical pulses intensities ranging from 0 to 0.10. For $B > 3.42$, a step in the optical intensity is observed. This means that for an injected optical pulse strength of 0.006 a response pulse is formed. For a gain bias current $A = 4.3$ and level of absorption $B = 3.42$, the threshold for an excitable response is almost six times lower compared to the case where $A = 4.3$ and $B = 3.72$, see Figure 3. Similar results can be achieved by tuning $A$ and setting $B$ to a specific fixed value. This means that depending on the biasing conditions, a response pulse can be formed only after a single small optical trigger is injected into the cavity.

A special case occurs when the value for $B$ is lowered even further, e.g. 3.32, a response is observed regardless the injected optical pulse strength. This means that the laser is able to form a pulse without any optical pulse injected, e.g. it is self-pulsating. This is a different operation regime compared to the excitable regime. Another special case is when multiple subthreshold pulses close in time are injected into the model. Due to the recovery rates, a short train of subthreshold pulses applied within the recovery period is also able to saturable the absorber and result in an excitable response.

Another aspect of the pulse formation is the time delay between the injected pulse and its response. Figure 4 shows the response amplitude after a first and second optical pulse injection. The time delay between the two pulses is varied from 0 to 140 $\tau_p$. The solid line shows the response after the first pulse is injected. This is a flat line, since the system is initially at a steady state. Note that for a second injected pulse, there is a dead time of about $\Delta t = 60$ $\tau_p$. During this window, the system has not recovered yet, i.e. the gain is not strong enough and losses are too high to form a pulse. After this window, a second pulse starts to form, although at a lower amplitude. If the time delay between the two pulses is increased further, both responses approach the same amplitude. The period during which a second pulse is formed, although at a lower amplitude, is defined as the relative refractory period, which is a similar property biological neurons show. This is an important factor, since it sets a lower limit on the time a second pulse can be formed.

## III. Fabricated Device

The gain and saturable absorber integrated laser was fabricated in a commercially available active-passive multi-project wafer (MPW) InP integration platform [30]. In this relatively mature platform, photonic integrated circuits can be designed using predefined building blocks such as gain sections, phase shifters, distributed Bragg reflectors (DBR), multimode interference reflectors (MIR), electrical isolation sections and 2.0 $\mu$m and shallow and 1.5 $\mu$m wide deeply-etched waveguides. In Figure 5, the cross-section of the two types of waveguides are shown. An InGaAsP multi quantum well (MQW) layer is used for active regions, surrounded by InP for passive components and waveguides. To probe the active regions electrically, layers of InGaAs and gold are deposited on top of the InP layer.

Using these building blocks, linear cavity lasers with an 80 $\mu$m saturable absorber, 500 $\mu$m gain section, a 500 $\mu$m phase shifter, a 350 $\mu$m DBR optimized for reflections at

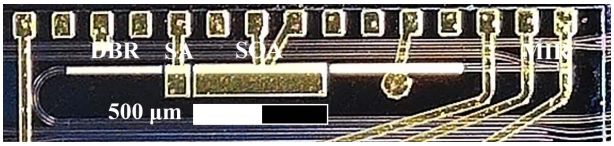


Fig. 6. Micrograph of one gain and saturable absorber laser.

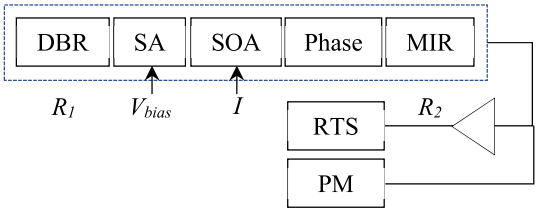


Fig. 7. Schematic overview of the measurement setup. DBR: distributed Bragg reflector, SA: saturable absorber, SOA: semiconductor optical amplifier, MIR: multimode interference reflector, RTS: real time scope, PM: power meter.

1550 nm and an MIR with estimated reflectivities of 0.87 and 0.40, respectively, were fabricated. The active regions are separated by 30 $\mu$m electrical isolations sections and are connected using shallow and deeply etched waveguides. The motivation for the chosen dimensions was to fabricate a laser that has the smallest form factor possible on this platform, and yet would be able to show excitability. This means that all individual components should be as small as possible. The gain section length was based on a Fabry-Pérot laser cavity comprising a 420 $\mu$m gain section and two multimode interference reflectors previously fabricated on the same platform [30]. To account for the photon absorption by the saturable absorber, a larger gain section and higher reflection DBR were used. The DBR length of 350 $\mu$m was chosen to ensure single mode operation and a relatively high reflectivity of approximately 0.8 [31]. The electrical isolation sections of 30 $\mu$m are chosen to yield high enough isolation between sections ($\sim$M$\Omega$). The outputs of the laser are coupled to the edge of the chip, where light can be collected using lensed fibers. An isolator prevents back reflections from the measurement equipment to the chip. Figure 6 shows a micrograph of one of the fabricated devices. Clearly visible are both mirrors, the folded waveguides going to the edges of the chip, the saturable absorber and gain sections, and a phase shifter.

## IV. Measurements

Figure 7 shows a schematic overview of the DUT and the measurement setup. The chip temperature was stabilized on a copper chuck using a Peltier element and ILX Lightwave 3900 TEC to a temperature of 20°C. Using a lensed fiber, light was collected at the MIR output of the chip, amplified by a Keopsys EDFA before it was fed into a high speed photodiode and 6GHz LeCroy Wavemaster 8600A real time oscilloscope to collect time traces. A power meter is used to monitor the optical output and to align the lensed fiber optimally to the edge coupler. The ILX Lightwave 3900 was also used to pump current into the gain section, a Keithley

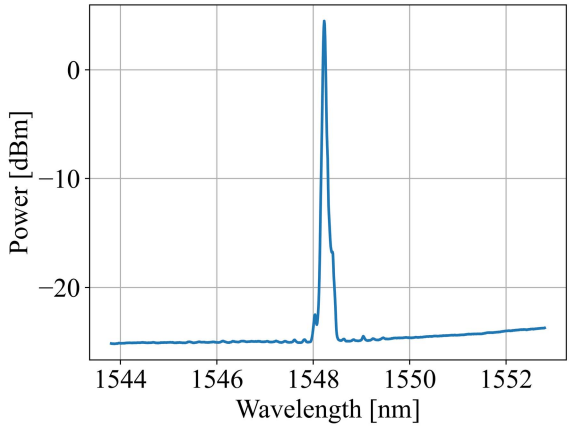


Fig. 8. Optical spectrum of a two-section laser operation above threshold after optical amplification.

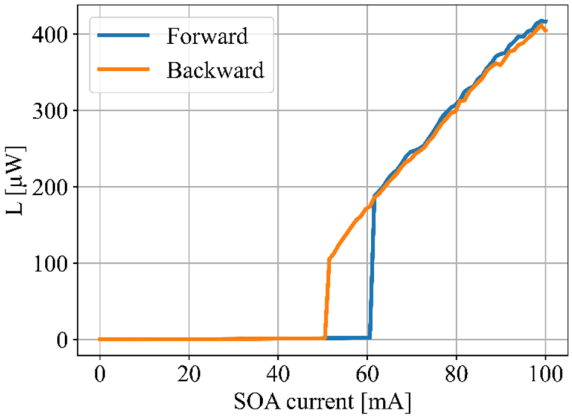


Fig. 9. L-I curve with hysteresis. The current is swept in the positive (blue) and negative (orange) direction. The instantaneous onsets around 50 and 60 mA are the result of the bistable character of the device.

2401 source meter unit (SMU) was used to apply a voltage and to measure the current through the saturable absorber.

The integrated laser showed single mode operation well above the lasing threshold, as shown in Figure 8. At the lasing threshold, the laser was operating in multimode regime.

To validate that our devices indeed show bistable operation, the L-I characteristics and saturable absorber I-V characteristics are measured first. In the L-I characteristics, the bistability manifests itself in a hysteresis when a fixed bias voltage or current is applied at the saturable absorber, while the current through the gain section is swept from low to high and vice versa [24]. Figure 9 shows a sudden onset in the optical output power in both gain current sweep directions. In this experiment, the current was swept from 0 to 100 mA in steps of 1 mA with a scan dwell time of 0.1 sec. The moment at which this sharp increase happens, depends on the direction the current is swept, and thus a hysteresis is observed. Although the maximum optical output power only reaches 400 $\mu$W, this was sufficient to observe the hysteresis and verify our device shows bistable operation.

The bistability is also present when the saturable absorber I-V characteristics are measured [24]. In Figure 10, the voltage

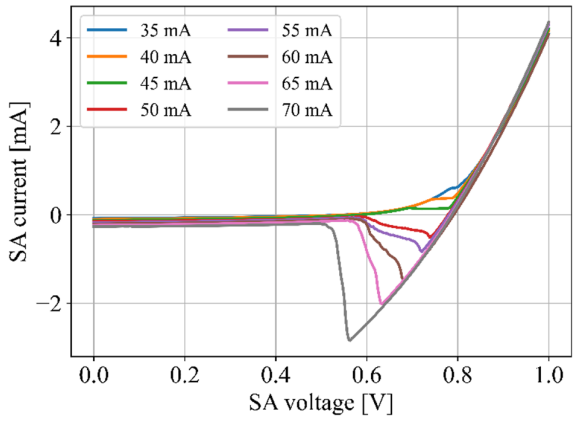


Fig. 10. Saturable absorber I-V characteristics.

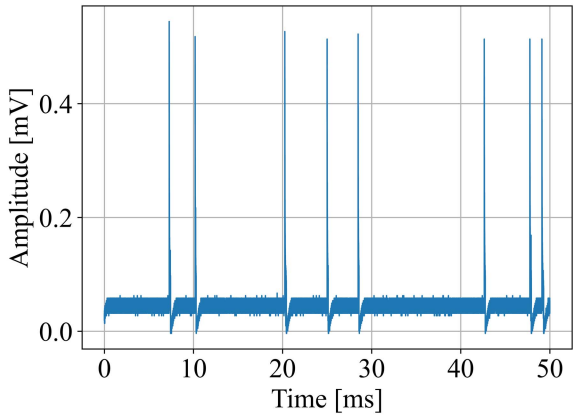


Fig. 11. Time trace at $V_{SA} = 0.727$ V, with $I = 50.11$ mA.

at the saturable absorber was swept from 0.0 to 1.0 V in steps of 0.01 V, while the current through the saturable absorber was monitored. This procedure was then repeated for 10 different gain pump currents. At a bias of 0 V, the absorption is relatively strong and stimulated emission in the cavity is suppressed. Increasing the positive junction voltage applied at the saturable absorber decreases the absorption, which increases stimulated emission. As a result, the photon density in the cavity increases and a larger negative photo current is generated. This is observed between approximately 0.5 V and 0.8 V for gain currents between 50 and 70 mA. In this case, the saturable absorber is bleached and the laser is turned on. When the voltage is further increased to a value above 0.8 V, the typical forward bias diode characteristic becomes dominant.

Next, the gain section is biased slightly below the hysteresis in Figure 9 at 50.11 mA. From simulations, it was found that at this biasing point excitable behavior is to be expected. Over 50 ms (1M samples), the optical output is monitored for different saturable absorber voltages. At a saturable absorber voltage of approximately 0.720 mV, the laser starts to generate pulses without any optical injection. By increasing the voltage only slightly, the absorption decreases and the density of pulses rises. This is clearly visible in Figure 11 and Figure 12 for voltages of 0.727 V and 0.730 V, respectively.

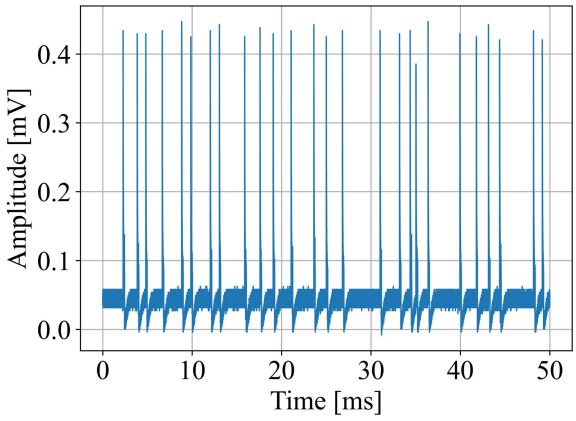


Fig. 12. Time trace at $V_{SA} = 0.730$ V, with $I = 50.11$ mA.

Note that the pulses do not occur at a fixed repetition rate, which would be expected for a self-pulsating laser.

Note that the pulses do not occur at a fixed repetition rate, which would be expected for a self-pulsating laser. Given the quasi-random character of the pulses and the fact that pulses occur on the millisecond timescale, we conclude that the pulses are not generated by self-pulsating mechanisms and relaxation oscillations, but that these pulses are likely triggered by noise.

## V. Noise Modeling

To model optical noise, a white-noise fluctuating $\delta$-correlated function (Langevin force) $F_I(t)$ is added to Eq. (3) in the normalized Yamada model as follows:

$$\frac{dI}{dt} = \gamma_I \left[G(t) - Q(t) - 1\right] I(t) + \epsilon f(G) + \theta(t) + F_I(t) \tag{4}$$

The equations for gain and absorption remain as in Eq. (1) and (2).

In (4), the Langevin force $F_I(t)$ satisfies [32]:

$$\langle F_a(t) \rangle = 0 \tag{5}$$

$$\langle F_I(t) F_I(u) \rangle = 2D_{II}\delta(t-u) \tag{6}$$

where $D_{II}$ is the diffusion coefficient for the intensify. In each integrated step, a random number is drawn from a Gaussian probability distribution with zero mean and standard deviation $2R_S I \Delta t$, where $R_s$ is the average of spontaneous emission rate and the fixed the integration timestep $\Delta t$.

The extended model with optical noise is used to simulate the optical output of a laser biased in the excitability regime. For weak absorption, in this case $B \leq 3.680$, noise is able to trigger the laser to create an irregular train of pulses. This is shown in Figure 13 and Figure 14 for values of $B = 3.6802$ and 3.6794, respectively.

From these figures is clear that by decreasing the absorption only slightly ($\Delta B = 0.0008$), the pulse density increases significantly. Similar results are obtained by changing the value for the gain $A$. By eliminating the noise, i.e. setting $R_s$ in both cases to zero, no pulses are generated. From

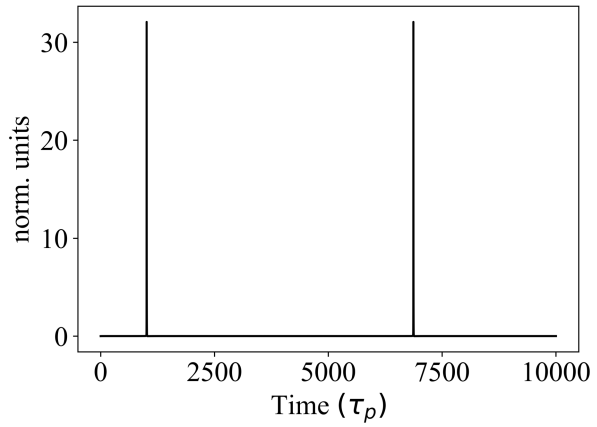


Fig. 13. Simulated time trace using $A = 4.5$, $B = 3.6802$, $\beta_{sp} = 0.0001$, $r_s = 0.2$.

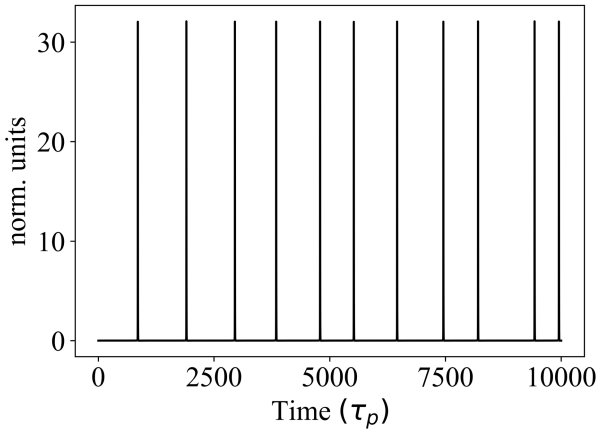


Fig. 14. Simulated time trace using $A = 4.5$, $B = 3.6794$, and $\beta_{sp} = 0.0001$, $r_s = 0.2$ to model the noise contribution.

these simulations it is clear that an external optical noise is able to trigger an excitable laser to generate an irregular train of pulses, similar to the measurements. Changing $B$ in simulations, which is similar to changing the absorber voltage, also changes the pulse density.

For a total of 50 simulated time traces with the parameter settings as in Figure 14, the timing distribution and its fit are shown in Figure 15. The timing follows a positively skewed distribution with a lower bound related to the relative refractory period dead-time. From simulations of multiple values of $B$, it is clear that the mean value decreases if $B$ is decreased, i.e. if the absorption becomes less, the time difference between consecutive pulses stabilizes.

## VI. Discussion

Integrated lasers with a saturable absorber and gain section share similar dynamical properties as biological neurons. For this reason, the proposed integrated laser might be a suitable candidate for an optical neuron. The biological neuron is highly optimized to operate in a noisy environment, therefore we have analyzed the effects of optical noise on an integrated two-section laser that can produce quasi-random spikes.

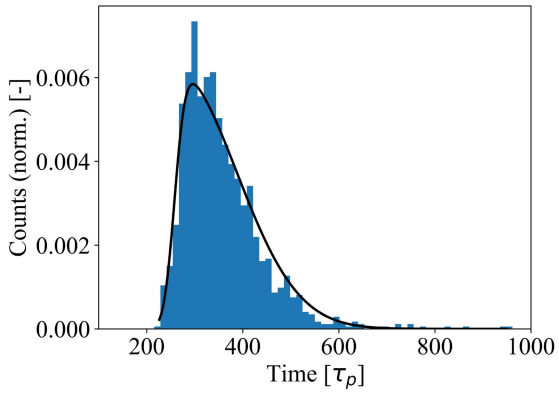


Fig. 15. Example of a simulated noise distribution of 1345 simulated pulses and the calculated positively skewed fit.

The normalized Yamada model has been used before to study excitability and describe the gain, absorber and intensity dynamics of optical neurons. With the extension described here, it is possible to study the effects of optical noise on the excitable laser. The qualitative agreement between the measurements and the data generated by the model indicates that noise may influence the spike generation when operated in the excitable regime. This is an important aspect to consider, especially when the integrated laser is used as an optical neuron.

## VII. Conclusion

In summary, we have measured and simulated a self-spiking saturable absorber and gain section laser. Integrated lasers show similar dynamical properties as biological neurons such as excitability and the relative refractory period, and might therefore be a suitable candidate to be used as an integrated optical neuron in an SNN. The laser dynamics were simulated first using the well-known Yamada model. A two-section laser was fabricated in a commercially available active-passive multi-project wafer (MPW) InP integration platform. The fabricated laser shows a bistability and hysteresis in the I-V and L-I characteristics, and shows a quasi-random self-spiking output on the millisecond timescale. An addition to the well-known Yamada model was presented to include the effects of optical noise on an excitable two-section laser, which is also an important aspect in biological neurons. This model shows qualitative agreement between absorption controlled simulated and measured spike densities.

## References

[1] P. R. Prucnal, B. J. Shastri, T. F. de Lima, M. A. Nahmias, and A. N. Tait, "Recent progress in semiconductor excitable lasers for photonic spike processing," *Adv. Opt. Photon.*, vol. 8, no. 2, p. 228, Jun. 2016, doi: 10.1364/AOP.8.000228.

[2] R. Stabile, G. Dabos, C. Vagionas, B. Shi, N. Calabretta, and N. Pleros, "Neuromorphic photonics: 2D or not 2D?" *J. Appl. Phys.*, vol. 129, no. 20, May 2021, Art. no. 200901, doi: 10.1063/5.0047946.

[3] M. A. Nahmias, B. J. Shastri, A. N. Tait, and P. R. Prucnal, "A leaky integrate-and-fire laser neuron for ultrafast cognitive computing," *IEEE J. Sel. Top. Quantum Electron.*, vol. 19, no. 5, pp. 1–12, Sep. 2013, doi: 10.1109/JSTQE.2013.2257700.

[4] C. Huang et al., "Prospects and applications of photonic neural networks," May 2021, *arxiv:2105.09943*.
[5] K. Boahen, "A neuromorph's prospectus," *Comput. Sci. Eng.*, vol. 19, no. 2, pp. 14–28, Mar. 2017, doi: 10.1109/MCSE.2017.33.
[6] M. Hejda, J. Robertson, J. Bueno, J. A. Alanis, and A. Hurtado, "Neuromorphic encoding of image pixel data into rate-coded optical spike trains with a photonic VCSEL-neuron," *APL Photon.*, vol. 6, no. 6, Jun. 2021, Art. no. 060802, doi: 10.1063/5.0048674.
[7] Y. Zhang, J. Robertson, S. Xiang, M. Hejda, J. Bueno, and A. Hurtado, "All-optical neuromorphic binary convolution with a spiking VCSEL neuron for image gradient magnitudes," *Photon. Res.*, vol. 9, no. 5, p. B201, May 2021, doi: 10.1364/PRJ.412141.
[8] J. Robertson, E. Wade, Y. Kopp, J. Bueno, and A. Hurtado, "Toward neuromorphic photonic networks of ultrafast spiking laser neurons," *IEEE J. Sel. Topics Quantum Electron.*, vol. 26, no. 1, pp. 1–15, Jan. 2020, doi: 10.1109/JSTQE.2019.2931215.
[9] J. Robertson et al., "Ultrafast neuromorphic photonic image processing with a VCSEL neuron," *Sci. Rep.*, vol. 12, no. 1, p. 4874, Dec. 2022, doi: 10.1038/s41598-022-08703-1.
[10] A. N. Tait, M. A. Nahmias, B. J. Shastri, and P. R. Prucnal, "Broadcast and weight: An integrated network for scalable photonic spike processing," *J. Lightw. Technol.*, vol. 32, no. 21, pp. 4029–4041, Nov. 1, 2014, doi: 10.1109/JLT.2014.2345652.
[11] V. Moskalenko, "Extended cavity passively mode-locked lasers in indium phosphide generic integration technology," Technische Universiteit Eindhoven, Eindhoven, The Netherlands, Tech. Rep., 2016.
[12] J. Robertson, M. Hejda, J. Bueno, and A. Hurtado, "Ultrafast optical integration and pattern classification for neuromorphic photonics based on spiking VCSEL neurons," *Sci. Rep.*, vol. 10, no. 1, p. 6098, Dec. 2020, doi: 10.1038/s41598-020-62945-5.
[13] H.-T. Peng et al., "Temporal information processing with an integrated laser neuron," *IEEE J. Sel. Top. Quantum Electron.*, vol. 26, no. 1, pp. 1–9, Jan. 2020, doi: 10.1109/JSTQE.2019.2927582.
[14] B. J. Shastri et al., "Photonics for artificial intelligence and neuromorphic computing," *Nature Photon.*, vol. 15, no. 2, pp. 102–114, Feb. 2021, doi: 10.1038/s41566-020-00754-y.
[15] L. Puts, W. Yao, and D. Lenstra, "Modeling a spiking optical neuron using normalized Yamada rate equations," in *Proc. 25th Annu. Symp. IEEE Photon.*, Benelux, Mons, Belgium, Nov. 2021, p. 4.
[16] A. N. Tait et al., "Neuromorphic photonic networks using silicon photonic weight banks," *Sci. Rep.*, vol. 7, no. 1, p. 7430, Dec. 2017, doi: 10.1038/s41598-017-07754-z.
[17] C. Wu, H. Yu, S. Lee, R. Peng, I. Takeuchi, and M. Li, "Programmable phase-change metasurfaces on waveguides for multimode photonic convolutional neural network," *Nature Commun.*, vol. 12, no. 1, p. 96, Dec. 2021, doi: 10.1038/s41467-020-20365-z.
[18] J. Feldmann, N. Youngblood, C. D. Wright, H. Bhaskaran, and W. H. P. Pernice, "All-optical spiking neurosynaptic networks with self-learning capabilities," *Nature*, vol. 569, no. 7755, pp. 208–214, May 2019, doi: 10.1038/s41586-019-1157-8.
[19] J. L. A. Dubbeldam, B. Krauskopf, and D. Lenstra, "Excitability and coherence resonance in lasers with saturable absorber," *Phys. Rev. E, Stat. Phys. Plasmas Fluids Relat. Interdiscip. Top.*, vol. 60, no. 6, pp. 6580–6588, Dec. 1999, doi: 10.1103/PhysRevE.60.6580.
[20] B. Krauskopf, K. Schneider, J. Sieber, S. Wieczorek, and M. Wolfrum, "Excitability and self-pulsations near homoclinic bifurcations in semiconductor laser systems," *Opt. Commun.*, vol. 215, nos. 4–6, pp. 367–379, Jan. 2003, doi: 10.1016/S0030-4018(02)02239-3.
[21] J. L. A. Dubbeldam and B. Krauskopf, "Self-pulsations of lasers with saturable absorber: Dynamics and bifurcations," *Opt. Commun.*, vol. 159, nos. 4–6, pp. 325–338, Jan. 1999, doi: 10.1016/S0030-4018(98)00568-9.
[22] R. Otupiri, B. Garbin, N. G. R. Broderick, and B. Krauskopf, "Excitability in an all-fiber laser with a saturable absorber section," *J. Opt. Soc. Amer. B, Opt. Phys.*, vol. 38, no. 5, p. 1695, May 2021, doi: 10.1364/JOSAB.420204.
[23] C. Harder, K. Y. Lau, and A. Yariv, "Bistability and pulsations in CW semiconductor lasers with a controlled amount of saturable absorption," *Appl. Phys. Lett.*, vol. 39, no. 5, pp. 382–384, Sep. 1981, doi: 10.1063/1.92745.
[24] C. Harder, K. Y. Lau, and A. Yariv, "Bistability and pulsations in semiconductor lasers with inhomogeneous current injection," *IEEE J. Quantum Electron.*, vol. QE-18, no. 9, pp. 1351–1361, Sep. 1982, doi: 10.1109/JQE.1982.1071711.
[25] R. Otupiri, B. Krauskopf, and N. G. R. Broderick, "The yamada model for a self-pulsing laser: Bifurcation structure for nonidentical decay times of gain and absorber," *Int. J. Bifurcation Chaos*, vol. 30, no. 14, Nov. 2020, Art. no. 2030039, doi: 10.1142/S0218127420300396.
[26] H. Kawaguchi, "Optical bistability and chaos in a semiconductor laser with a saturable absorber," *Appl. Phys. Lett.*, vol. 45, no. 12, pp. 1264–1266, Dec. 1984, doi: 10.1063/1.95120.
[27] U. Keller, *Ultrafast Lasers: A Comprehensive Introduction to Fundamental Principles with Practical Applications*. Cham, Switzerland: Springer, 2021, doi: 10.1007/978-3-030-82532-4.
[28] J. Javaloyes and S. Balle, "Mode-locking in semiconductor Fabry–Pérot lasers," *IEEE J. Quantum Electron.*, vol. 46, no. 7, pp. 1023–1030, Jul. 2010, doi: 10.1109/JQE.2010.2042792.
[29] C. Gordon, M. Cumbajin, G. Carpintero, E. Bente, and J. Javaloyes, "Absorber length optimization of on-chip colliding pulse mode-locked semiconductor laser," *IEEE J. Sel. Topics Quantum Electron.*, vol. 24, no. 1, pp. 1–8, Jan. 2018, doi: 10.1109/JSTQE.2017.2759263.
[30] M. Smit et al., "An introduction to InP-based generic integration technology," *Semicond. Sci. Technol.*, vol. 29, no. 8, Jun. 2014, Art. no. 083001, doi: 10.1088/0268-1242/29/8/083001.
[31] D. Zhao, "High-precision distributed Bragg reflectors in a generic photonic integration platform," Technische Universiteit Eindhoven, Eindhoven, The Netherlands, Tech. Rep., 2018.
[32] G. H. M. van Tartwijk and D. Lenstra, "Semiconductor lasers with optical injection and feedback," Dept. Phys. Astron., Free Univ., Amsterdam, The Netherlands, 2021, doi: 10.1088/1355-5111/7/2/003.

**Lukas Puts** was born in Nijmegen, The Netherlands, in 1994. He received the M.Sc. degree (cum laude) in photonic integration from the Eindhoven University of Technology in 2020, where he is currently pursuing the Ph.D. degree in photonic spiking neural networks.

**Daan Lenstra** (Life Senior Member, IEEE) was born in Amsterdam, The Netherlands, in 1947. He received the M.Sc. degree in theoretical physics from the University of Groningen and the Ph.D. degree from the Delft University of Technology.

Since 1979, he has been researching topics in quantum electronics, physics of lasers, and condensed matter. He is currently an Emeritus Professor with the Photonics Integration Group, Eindhoven University of Technology. He has over 300 scientific publications on various topics, mostly on semiconductor lasers and nonlinear laser dynamics.

**Kevin Williams,** biography not available at the time of publication.

**Weiming Yao** (Member, IEEE) received the dual M.Sc. degrees in photonic networks engineering from Aston University, U.K., and Scuola Superiore Sant'Anna, Italy, in 2012, working on optical signal processing in fibre, performed at Osaka University, Japan.

At the Eindhoven University of Technology (TU/e) he explored high-capacity and high-density integrated optical transmitters, leading to the Ph.D. degree in 2017. Since then, he has continued to work at TU/e on photonic integrated circuits. He has a background in both photonic networks and devices with a particular focus on high-speed and high-density component integration and its connection to electronics. Since 2020, he has been an Assistant Professor with the Electrical Engineering Department, TU/e. He was a recipient of an NWO Veni grant to work on neuromorphic photonics.